Soft Matter

ROYAL SOCIETY OF CHEMISTRY

PAPER

View Article Online
View Journal | View Issue

Cite this: *Soft Matter*, 2022, **18**, 5509

Received 6th March 2022,
Accepted 16th June 2022

DOI: 10.1039/d2sm00305h

rsc.li/soft-matter-journal

Single-walled carbon nanotube reptation dynamics in submicron sized pores from randomly packed mono-sized colloids†

Zhao Tang,[a] Shannon L. Eichmann,[a] Brahim Lounis,[bc] Laurent Cognet,[bc] Frederick C. MacKintosh[adef] and Matteo Pasquali *[adg]

Studying the Brownian motion of fibers and semi-flexible filaments in porous media is the key to understanding the transport and mechanical properties in a variety of systems. The motion of semi-flexible filaments in gel-like porous media including polymer networks and cell cytoskeleton has been studied theoretically and experimentally, whereas the motion of these materials in packed-colloid porous media, advanced foams, and rock-like systems has not been thoroughly studied. Here we use video microscopy to directly visualize the reptation and transport of intrinsically fluorescent, semiflexible, semiconducting single-walled carbon nanotubes (SWCNTs) in the sub-micron pores of packed colloids as fixed obstacles of packed-colloid porous media. By visualizing the filament motion and Brownian diffusion at different locations in the pore structures, we study how the properties of the environment, like the pore shape and pore structure of the porous media, affect SWCNT mobility. These results show that the porous media structure controls SWCNT reorientation during Brownian diffusion. In packed-colloid pores, SWCNTs diffuse along straight pores and bend across pores; conversely, in gel pores, SWCNTs consistently diffuse into curved pores, displaying a faster parallel motion. In both gel and packed-colloid porous media, SWCNT finite stiffness enhances SWCNT rotational diffusion and prevents jamming, allowing for inter-pore diffusion.

Introduction

For confined fibers and semiflexible filaments, Brownian motion perpendicular to the filament motion is significantly suppressed in porous media where anisotropic filament motion in curvilinear confining tubes results in snake-like reptation in pores. Reptation theory was originally developed to describe polymer diffusion and the resulting stress relaxation in polymer melts[1–4] but has been successful at describing the dynamics of stiff or semiflexible polymer solutions,[5–7] as well as filament motion in more complex confining potentials.[8,9]

Semiflexible chain Brownian motion in submicron sized porous media is a core research topic to understand the mechanism of microfluidic separation[10–12] and nanoparticle tracer dispersion.[13] Among various porous media with submicron sized pores, gels and packed colloids are two of the most widely used kinds. Gel-like porous media for biological applications[8,10–12] have been intensively studied. The experiments by Fakhri *et al.*[14] on SWCNTs in agarose gels show that even a small bending compliance of a SWCNT dramatically enhances rotational diffusion, consistent with Odijk's prediction of a characteristic relaxation time $\tau_r \sim L^2 L_p$ that is independent of pore size and depends on the chain length L and persistence length L_p. In addition, recent microrheology experiments indicate accelerated rotation from thermal bending of the component polymer chain in gel-like porous media.[15,16] These and other studies demonstrate the use of single filament imaging to understand how the properties of the surrounding confining media affect filament behavior.[7,14,17,18]

While several studies in gel-like porous media for biologically relevant media exist,[19–22] there are only a few simulation studies of the molecular diffusivity of single semiflexible or rod-like filaments in packed colloids,[13,23] let alone experiment.[18] Direct extension of Brownian motion from the gel pores to packed colloid pores is not straightforward due to pore

---

[a] *Department of Chemical and Biomolecular Engineering, Rice University, Houston, Texas 77005, USA. E-mail: mp@rice.edu*
[b] *Laboratoire Photonique Numérique et Nanosciences, Université de Bordeaux, LP2N, F-33405 Talence, France*
[c] *Institut d'Optique and CNRS, LP2N, F-33405 Talence, France*
[d] *Department of Chemistry, Rice University, Houston, Texas 77005, USA*
[e] *Center for Theoretical Biological Physics, Rice University, Houston, TX 77030, USA*
[f] *Department of Physics and Astronomy, Rice University, Houston, Texas 77005, USA*
[g] *Department of Materials Science and NanoEngineering, The Carbon Hub, The Smalley Institute for Nanoscale Science and Technology, Rice University, Houston, Texas 77005, USA*

† Electronic supplementary information (ESI) available. See DOI: **https://doi.org/10.1039/d2sm00305h**

structure differences. First, the packed-colloid pores have a much higher volume fraction ($\sim$60 v/v%) of solid than similarly sized gel pores (0.5–2.0 v/v%). This much higher solid content could contribute to less tortuous pore structures.[24] Second, pores produced by packed colloids are essentially fixed for semiflexible rods to move within, while, based on a previous microscopy study in gel pores, the gel path fluctuates and SWCNTs bend to generate the diffusion path.[14] Third, randomly packed mono-sized colloids produce a wide pore size and shape distribution,[25] leading to higher pore heterogeneity than that in gel pores. Applications such as filtration and tracer studies[26] utilize packed colloids as porous media, where these studies track the molecular concentration in the effluent stream to infer mobility. Single particle tracking of rigid rod-like bacteria in packed-colloid pore systems reveals trapping and hopping motion at different pore locations.[27] As such, these studies do not directly address the physics of single stiff, yet semiflexible, filament mobility in packed-colloid confining media. Finally, it is not known how semiflexible filament mobility in a gel-like porous media compares to transport in packed-colloid porous media, which is directly relevant to studies of molecular transport in chromatography, where both gel-like[28] and packed-colloid porous systems[11,12] are used.

Here, we apply near infrared video microscopy to directly study semi-conducting SWCNT diffusive behavior and bending dynamics in porous media at the single-SWCNT level. Convective self-assembly[29,30] is used to create a pore space of packed colloids, with a tunable average pore size of 57%, the colloid diameter in close packed areas.[25] By controlling the assembly rate, we generate both randomly packed and ordered regions to study the effects of the pore structure in the same experimental system. We simultaneously track center of mass (COM), orientation θ, and bending angle ϕ to study SWCNT Brownian motion in the pores between packed colloids and compare this behavior with the mobility of SWCNTs in gel-like porous media.[14,20,21] In addition, we study the heterogeneity of the packed colloids on Brownian motion and molecular reptation. We find that, at locations with several pores of accessible orientations, SWCNTs rotate between multiple straight pores and display normal rotational diffusion. Conversely, at locations with few accessible pores, SWCNTs' rotation is confined and thus SWCNTs show subdiffusive behavior.

Experimental section

Sample preparation

We use a solution of (6,5) chirality enriched single walled SG65i SWCNTs (Southwest Nanotechnologies) in a 1% weight sodium deoxycholate (DOC, G-biosciences deoxycholic acid sodium salt, >99% purity) solution. The solution is prepared by speedmixing 1 mg of SWCNTs per 1 mL 4% weight DOC solution for 48 h, followed by centrifuging at 13.4 krpm for 2 h (Eppendorf minispin centrifuge). Then the supernatant DOC concentration is diluted to 1 wt% for further processing. The protocol from Gui[31] is used to selectively obtain long SWCNTs (>5 μm). Briefly, we add 4 wt% polystyrene sulfonate (PSS, average molecular weight $\sim$70 000 g mol^{-1}, Aldrich) in water to the supernatant after centrifugation to reach a total concentration of 1 wt% PSS in solution. This procedure selectively precipitates long SWCNTs from the solution. The 1 wt% PSS mixture is then centrifuged at 13.4 krpm for 1 minute. The centrifuged pellet is dispersed in 1 wt% DOC solution to obtain long SWCNTs.

Measurements of unconfined chains are performed in a slit pore. A 0.5 μL drop of SWCNT DOC suspension is placed on a large coverslip (Gold Seal, thickness #1, 40 × 24 mm) and a small coverslip (Gold Seal, thickness #1, 18 × 18 mm) is gently placed on top to avoid trapped bubbles in the imaging cell. This forms a quasi-2D imaging chamber that is $\sim$2 μm thick. The edges of the small coverslip are sealed with epoxy (Hardman Double Bubble Red Extra Fast Epoxy) to prevent convective flow caused by evaporation.[29,30] The following procedure is used for preparing imaging cells with packed colloids. First, a concentrated solution of silica particles (1.97 μm diameter, Bangs Labs, 10 v/v%) is prepared by centrifugation and disposal of the excess water leaving behind a centrifuged pellet of concentrated silica particles. Next, the silica particle-SWCNT solution is prepared by mixing 1 μL of DOC SWCNTs with 5 μL of the centrifuged pellet. Finally, the imaging cell is prepared by sandwiching a 5 μL drop of the prepared silica particle-SWCNT solution between two microscope coverslips to form a quasi-2D cell as described above. Prior to sealing the cell with epoxy, however, the sandwiched cell is allowed to rest for a few minutes to allow colloid packing.

NIR microscopy setting

NIR microscopy is performed using a Nikon Ti-E inverted microscope in combination with a liquid nitrogen cooled 2D-OMA InGaAs NIR camera from Roper Scientific.[32] The camera in the transmitted light mode is capable of capturing the morphology of silica colloids (Fig. 2(a)). SWCNT fluorescence is excited by a 660 nm external diode laser (Newport LQC660-110C, 110 mW). To selectively visualize only (6,5) chirality SWCNTs, a 980 nm wavelength, 10 nm bandpass filter (Edmund optics #65186) is used. Videos of the SWCNT motion are collected with a Nikon PlanApo 100×/1.40 N.A./0.13 W.D. oil immersion objective and 1.5× magnification at 15.7 fps and a 50 ms exposure time.

Image analysis

An automated image analysis MATLAB code is developed to extract backbone points, orientation (θ), and center of mass (COM) frame-by-frame from the NIR microscopy video. Orientation and COM are determined from ellipse fitting[14] and illuminating pixel point location (built-in MATLAB function). Rotational and translational diffusion coefficients cannot be evaluated easily because multiple diffusion categories, such as subdiffusion and normal diffusion, are involved in this system. The widespread time interval power-law index makes the diffusion coefficient unit inconsistent. Here, we use an MSD (δ^2) at

t time with an interval of 1 second to evaluate the diffusion rate at different times with equation:

$$\delta\chi^2(t) = (\chi(t + 0.5s) - \chi(t + 0.5s))^2 \qquad (1)$$

For comparison convenience between different time spots, spontaneous MSD is normalized by the time average of MSD, which is defined commonly as time-averaged MSD (TA-MSD, $\delta^2/\langle\delta^2\rangle$) in the literature.

The bending angle ϕ is extracted from the end-point tangent vectors of a fit rotated parabola to the SWCNT backbone. To obtain optimal parabola rotation with the smallest error, the MATLAB minimal search function fminsearch is used to find the parabola rotation angle with a minimal normalized residual error after rotation. We define the bending angle ϕ as the difference between the tangential angles at the ends of the rotated fit parabola. The backbone points extraction procedure uses the protocol by Gittes.[33]

Results and discussion

SWCNT Brownian motion in packed-colloid pores

Randomly packed colloid pores have a complicated pore structure and size distribution. Fig. 1(a) and (b) illustrate the pore structure of two types of media: packed colloids and a gel, respectively. The pore space in packed-colloid (grey area) has a complex structure with wide compartments (*i.e.*, pore body, green sphere in Fig. 1(a)) and narrow connectors (*i.e.*, pore throat, blue sphere in Fig. 1(a)) between compartments. Based on the particle packing protocol, the monosized colloids used to form the porous media are tens of layers thick with an approximate average pore size ξ_a of 0.57 times the colloid diameter[34] and average pore throat size ξ_t is 0.19 times the colloid diameter.[35] Fig. 1(b) shows a gel-like porous structure. Compared to colloid packing pores, gel-like pores have a lower solid volume fraction, higher porosity, higher transparency and higher homogeneity.

In this experiment, we use SWCNTs with length ranging from 3 to 12 μm in randomly packed multiple layers of monosized colloids (Fig. 2(a)). Fig. 2(b) shows the morphology of this randomly packed pores from 2 μm diameter colloids. The porous media generated with 2 μm diameter packed colloids have a 1.14 μm average pore size with a 0.38 μm pore throat size. Inset fluorescence images show reptation of a ~7.0 μm SWCNT diffusing between several straight pores with different orientations. Tracked SWCNT COMs show the tortuous porous structure in packed-colloid pores. SWCNT fluorescence images show conformations during diffusion. In single straight pore confinement, SWCNT (second and fourth marked point from left in Fig. 2(b)) completely align with the pore orientation. While diffusing across two pores (first and third marked point from left), SWCNT's moderate flexibility enables quick chain bending across pores. This flexibility enabled bending across pores is also observed in the gel-like porous structure.[14]

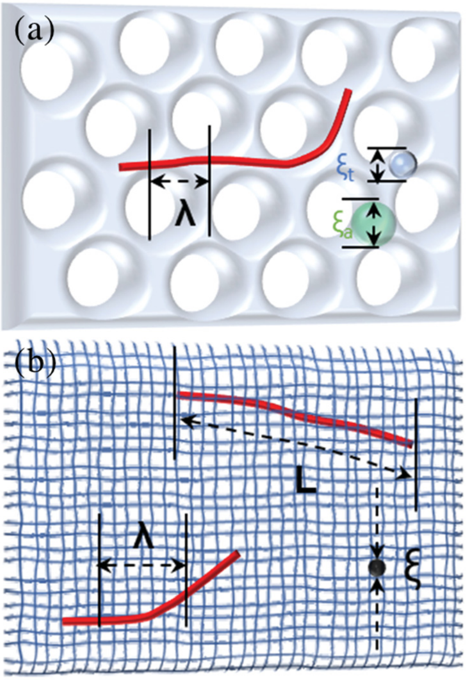

Fig. 1 Structure comparison between (a) randomly ordered packed-colloid pores of this work and (b) agarose gel pore systems. (a) Packed particles have high solid (grey sphere) volume percentage (~60 v/v%) and low porosity (~34 v/v%), and are translucent to opaque depending on media thickness. Representative pore is drawn with the light grey volume where ξ_a and ξ_t represent the average pore size and average pore throat size. (b) Porous media produced by agarose gels have a low solid (blue curved lines) volume (0.5–2.0 v/v%), high porosity (>98 v/v%), and are transparent. In the gel-like porous media system only one pore size exists where ξ corresponds to ξ_a in packed-colloid pores. Long semiflexible filaments (red curved lines) are drawn in each with contour length L to display the deflection length λ.

With COM and orientation tracking from fluorescence microscopy in Fig. 2, we can further study SWCNT rotational and translational Brownian motion at different lag times with mean square displacement (MSD) and mean square angular displacement (MSAD) in packed-particle pores.[36]

Over short time scales, a given SWCNT diffuses freely without being affected by its porous surroundings. After the SWCNT entangles with a single pore, it diffuses back and forth along the pore. All non-aligned motions with pore orientation are frozen, including perpendicular motion and rotation. The average time of a SWCNT being confined is defined as the entanglement time τ_e. In this experiment, the frame time (50 ms) is shorter than the estimated entanglement time (around 1 s). When the SWCNT probes more than one straight pore, the SWCNT bends to diffuse into the new pore. The disentanglement time τ_d is the average time it takes for the SWCNT to diffuse out of one pore. This reptation motion is reflected in the SWCNT Brownian motion as shown in Fig. 3. At a time longer than the rotation time $\tau_r = 1/(2D_r)$, the SWCNT loses its memory of initial orientation, and the diffusion becomes isotropic, which is well-described by Perrin-Smoluchowski theory.[37]

Fig. 3(a) shows SWCNT rotational dynamics in particle random packing pores. At short times, between entanglement time τ_d and disentanglement time τ_d, the MSAD displays a

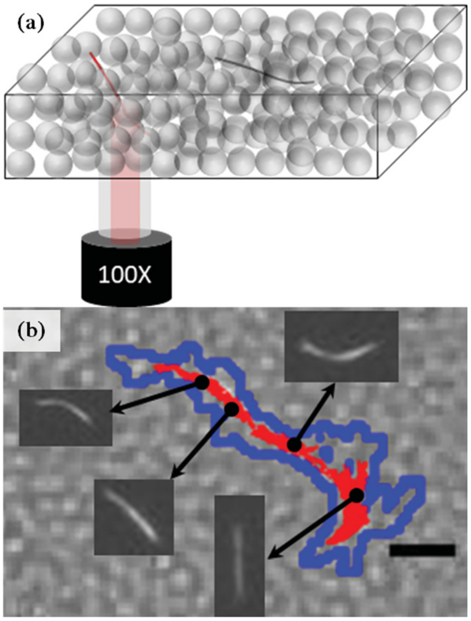

Fig. 2 Experimental settings of semiflexible filament molecule, SWCNT, diffusion (red curved line) in randomly packed silica colloid (grey beads) pores. (a) Illustration of single molecule microscopy. Surfactant-wrapped SWCNTs dispersed in a silica colloid filled glass imaging cell. (b) SWCNT travel area (blue line) and COM (red) overlap with the bright-field image of the 2 μm in diameter randomly packed colloids. Inset images show the configuration of SWCNT at marked locations. Scale bar 5 μm.

subdiffusive regime with the power law index being smaller than one. However, above the disentanglement time τ_d, SWCNT rotation follows normal diffusion with a temporal exponent of one. Translational Brownian motion is studied after decomposing SWCNT motion as parallel s and perpendicular n to the SWCNT molecular axis, shown in Fig. 3(b). At short times during in-pore diffusion ($\tau_e < \tau < \tau_d$), perpendicular diffusion is frozen as shown by the plateau in the MSD. The parallel motion at short times still displays subdiffusive behavior with a 3/4 power law index from SWCNT chain thermal bending,[36,38–40] which is the same behavior observed when SWCNTs diffuse into gel pores.[14] At longer time ($\tau > \tau_d$), cross-pore diffusion occurs and both parallel and perpendicular translational Brownian motion are once again the same as in the case of SWCNT diffusing in gel pores. The disentanglement time τ_d is marked on both MSD and MSAD curves (Fig. 3) to show the coupled SWCNT rotational and translation diffusion in packed colloid pores. At the cross-pore time interval ($\tau > \tau_d$), the perpendicular MSD shows a super diffusive regime (exponent >1) due to coupling between rotational and translational motion when the SWCNT diffuses out of a single pore.

In all cases of SWCNT rotation in packed-colloid pores, the exponent of the MSAD changes at around 1.0 second, which is the entanglement time τ_e required for the filament motion to feel the hindrance caused by the pore surface.[41] Before entanglement, the SWCNT explores the pore structure which has a wide pore size distribution that corresponds to a wide distribution of entanglement times. Thus, MSAD curves before the entanglement time show a complex pattern from averaged entanglements. To study the rotational dynamics of entanglement ($\tau_f < \tau < \tau_e$), we sample a subset of the data during a straight pore confinement event. From the MSAD obtained from single pore confinement (green data, Fig. 3(a)), the entanglement time τ_e and rotation confinement $\langle \Delta\theta_0{}^2 \rangle$ can be estimated by assuming a single-exponential model for the MSAD, with $\langle \Delta\theta^2(\tau) \rangle = \langle \Delta\theta_0{}^2 \rangle (1 - e^{-\tau/\tau_e})$. Note that the entanglement time τ_e effect is not observed in the MSAD curves of the reported SWCNTs diffusing in gel pores.[22] The expected entanglement time ($\tau_e \propto \xi^2/D_\parallel \approx 0.04$ s) in the agarose gel system used to produce gel-like porous media from the prior study[14] cannot be captured due to the temporal resolution of the video microscopy experiments. To show the consistency of SWCNT Brownian dynamics scaling law in packed-colloid pores, we have plotted averaged MSD and MSAD of (6,5) chirality SWCNT with the same length at different locations

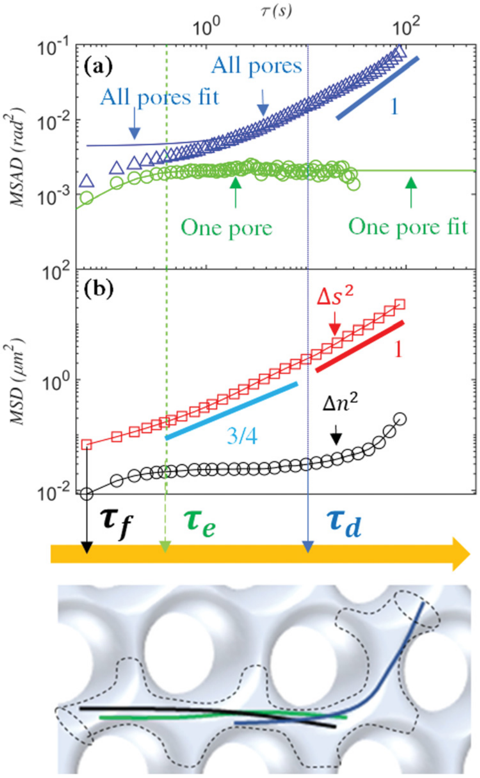

Fig. 3 SWCNTs' Brownian dynamics in randomly packed mono-sized colloid pores. (a) Rotational dynamics in multi-pores (All, blue) and single straight pore (SP, green). Curve fitting on the straight pore and multi-pores of MSAD data to extract entanglement time (τ_e) from single pore (SP) and disentanglement time (τ_d) from all data. (b) Parallel (Δs^2) and perpendicular (Δn^2)) translation Brownian dynamics showing three time-scales: τ_f is frame time, τ_e is entanglement time from (a), and τ_d is disentanglement time. τ_d plotted here is obtained by equation $\tau_d = \langle \Delta\theta_0{}^2 \rangle / (2D_r)$ with parameters from fitting MSAD all sample data (blue). Bottom figure shows SWCNT status with increasing lag time. Black molecule is the initial state. Green molecule first gets entanglement of pore. Dark blue molecule has diffused into a new pore. This same (6,5) chirality SWCNT 9.8 μm long and a 27 μm persistent length is shown in Fig. 3, 5, 6, 7. The bottom diagram shows the SWCNT behavior at the corresponding time interval in the same colour as the vertical time-scale marker arrows.

of randomly packed 2.0 μm diameter colloid pores in Fig. S1 of the ESI.† We find that the MSAD and MSD scaling laws are consistent with that displayed in Fig. 3.

SWCNT flexibility enhanced diffusion in packed-colloid pores

The rotational diffusion coefficient Dr is extracted from the MSAD curves by fitting the data with the equation $\langle\Delta\theta^2(\tau)\rangle = 2D_r\tau + \langle\Delta\theta_0{}^2\rangle$. For SWCNTs of this length range confined in the randomly ordered packed-colloid pores, the estimated entanglement time τ_e is around 1 second. For simplicity of extracting rotational diffusivities from the MSAD, only MSAD data with a lag time longer than the estimated entanglement time are used for the rotational diffusion coefficient analysis. The disentanglement time τ_d can be estimated using the equation $\tau_d = \langle\Delta\theta_0{}^2\rangle/(2D_r)$ by fitting the results above. It should be noted that two kinds of observations have been neglected. The first case is subdiffusion rotation with R-squared ($R^2 < 0.99$). The disentanglement time of this kind is too long to be observed using these experimental settings. The second case is negative rotational confinement $\langle\Delta\theta_0{}^2\rangle$ obtained from fitting the MSAD data. In this case, rotational confinement $\langle\Delta\theta_0{}^2\rangle$ is too small to be observed by direct curve fitting.

Since porous media from colloidal packing provides SWCNT confinement, it is interesting to examine whether the SWCNT finite stiffness can enhance rotational diffusion, following Odijk's theory,[41] or show confined behavior as in Doi-Edwards' theory for completely rigid rods.[1] Fig. 4(a) shows a master curve of $D_rL^2L_p/(k_BT/\eta)$ *versus* L/λ including both published results for SWCNT diffusion in gel pores and our new results in pores formed with packed colloids of different sizes. The blue and red data shown in the master scatter plot show that SWCNT motion in packed-colloid pores distributes around the Odijk's theory line as in the previous case for SWCNTs in gel-like pores (shown in green). The packed-particle pores data, however, show a wider scatter than those of gel pores, likely due to the higher pore heterogeneity.

Diffusing semiflexible chains in a gel-like porous media displays a linear relationship between disentanglement time τ_d normalized by its deflection length, λ, and filament contour length ($\tau_d/\lambda^2 \sim L$).[14,41] In packed-colloid pores, we expect the same linear relationship. Fig. 4(b) shows normalized disentanglement time τ_d/λ^2 verses SWCNT length L in packed-colloid pores obtained from the ellipse fitting method. Rather than a strong linear correlation as seen in the gel pores ($R^2 = 0.91$),[14] we observe a weak linear relationship with a $R^2 = 0.14$ correlation factor. This is related to additional heterogeneous factors that affect SWCNT mobility in packed-particle pores. Specifically, in addition to deflection length λ and contour length L, the semiflexible chain disengagement time τ_d in colloids packed pores is affected by the pore junction size and available angular paths[41,42] which are highly location-dependent in randomly packed colloids. As such, the resulting diffusion can be thought of as occurring on a rough energy landscape. In addition to the spatial heterogeneity of the medium, however, the energy landscape also depends on the conformation of the SWCNTs. These effects are likely the cause of the greater spread of our measured disentanglement time in packed-colloid pores as compared to that observed in gel pores.

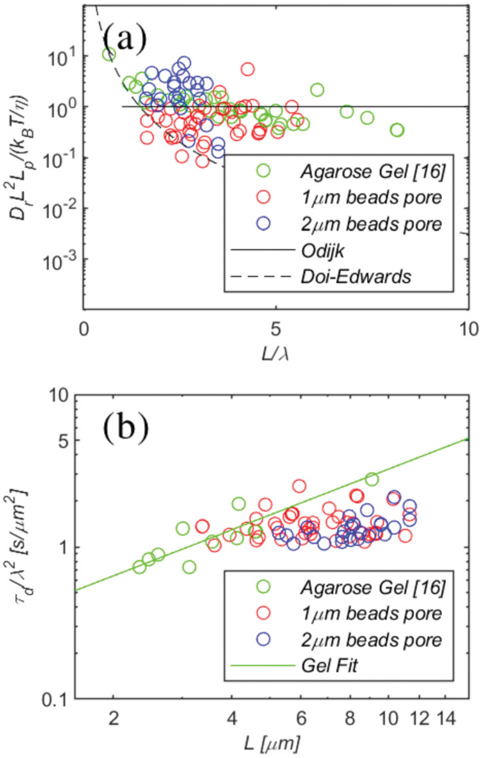

Fig. 4 Quantification of the SWCNT rotation rate in packed-colloid pores. (a) Normalized rotational diffusion coefficient for SWCNTs in packed-colloid pores and gel pores. (b) Normalized disengagement time (τ_d/λ^2) obtained shows a very weak relationship with the SWCNT length (correlation factors are 0.14 and 0.60 for packed-particle pores produced by 1 μm diameter and 2 μm diameter colloids, respectively) due to pore heterogeneity and rotational confinement from packed-colloid pores. Data from prior work with gel-like porous media are shown in green.

Pore heterogeneity effect on SWCNT Brownian motion

In randomly packed-colloid porous media, the pore orientation θ, pore throat size ξ_t, and pore size ξ_a are location dependent (Fig. 5(a)).[35] Hence, the SWCNT Brownian motion inside such porous media shows location-dependent dynamics due to structural heterogeneity. To study the pore heterogeneity effects, a single SWCNT is studied at five different locations in the packed-colloid pores where the orientation (Fig. 5(a)) and COM (Fig. 5(c)) are tracked at every frame. The MSAD is calculated to quantify the rotational dynamics that reflects the heterogeneity in angular confinement. In observation 5 (magenta data), the SWCNT bends to access multiple straight pores (>3) with distinct pore orientations (Fig. 5(a) and (b)). Thus, the MSAD (Fig. 5(b)) resembles the rotational dynamics in gels.[14] The disengagement time (τ_d) is the average time required for SWCNTs to travel across pores. At short times ($\tau < \tau_d$), the MSAD shows a sub-diffusive relationship (slope < 1) with a time lag, while at long times ($\tau > \tau_d$), the MSAD shows a diffusive relationship (slope = 1) with a time lag. In observations 1 and 2 (red and green traces), the orientation of the

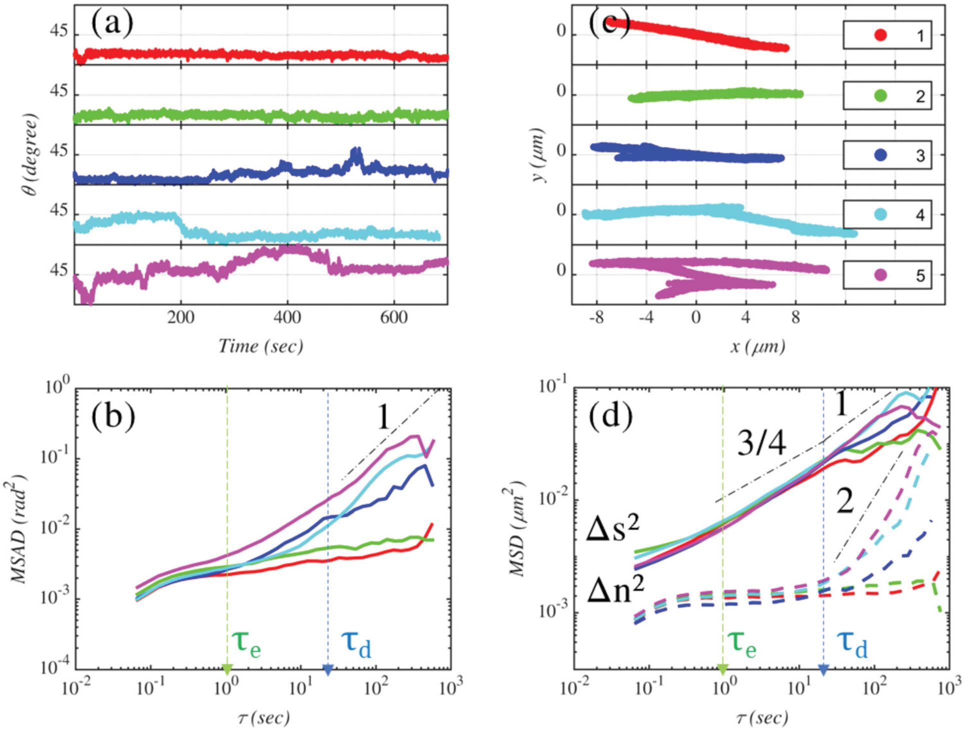

Fig. 5 Pore location dependent SWCNT dynamics of the same SWCNT. Colours represent five observations at different locations in packed-colloid pores. (a) Orientation tracking over frames. Each grid has a 200 second width and a 45 degree height. (b) Center of mass tracking from five videos. Each grid has 4 μm width and height. (c) Mean square angular displacement (MSAD) results from tracking orientation data. (d) Mean square displacement (MSD) parallel (Δs^2, solid line) and perpendicular (Δn^2, dashed line) to the projected SWCNT motion.

SWCNTs changes minimally during the observation, *i.e.*, the SWCNTs only reptate within the original straight pore during the video. This high level of confinement yields a sub-diffusive rotation. The remaining observations, where the SWCNTs diffuse into a single pore for the majority of the time but briefly sample other pores by bending, show a mixed MSAD effect between these two limit regimes.

As for the effect of pore heterogeneity on translational Brownian motion, we calculate the MSD parallel and perpendicular to the SWCNTs (Fig. 5(d)). Due to the coupling between rotational and translational motion, the entanglement time τ_e and disentanglement time τ_d can be clearly observed from the MSD of the motion perpendicular (dashed lines) to the SWCNT backbone. When confined to a single straight pore, as for observations 1 and 2, the MSD perpendicular to the SWCNT backbone Δn^2 shows a location-independent plateau between the entanglement time τ_e and the disengagement time τ_d. This is different from the gel case where the perpendicular MSD shows a 3/4 power law dependence on the lag time, which indicates thermal fluctuation dominated perpendicular motion. For colloidal packings, the broad distribution of pore diameters and the rigidity of the medium appear to effectively suppress transverse motion within a given pore. On longer time scales the MSD perpendicular to the initial backbone shows a super-diffusive regime, corresponding to inter-pore diffusion. Moreover, the widespread transition times between these regimes indicate a wide distribution of disentanglement times for a given SWCNT in different pore environments.

SWCNT reptation motions in packed-colloid porous media

To study the effect of pore heterogeneity, we tracked SWCNT bending and transport at different locations in packed-colloid pores. SWCNTs' finite flexibility introduces molecular bending when diffusing across two pores with different orientations. We track this effect *via* the bending angle ϕ. For simplicity, we fit the SWCNTs with a rotated quadratic polynomial. The positive bending angle is defined as the counter clock-wise bend when observing the molecule from left to right. The SWCNT bending angle is used to infer the local pore curvature without directly measuring the colloid pore structure. Fig. 6(a) shows the bending angle of a ∼10 μm SWCNT diffusing through a transition from one pore (red area in Fig. 6(a)) to the next straight pore (cyan area Fig. 6(a)) in the same experiment reported in Fig. 7 in randomly packed-colloid pores (average pore size 1.14 μm). In this observation, an average SWCNT bending angle of 42 degree occurs at the transition of the initial pore (red peak in Fig. 6(b)) and the average angle of 8 degrees is at the straight end of the pore (cyan peak in Fig. 6(b)). The SWCNT first reptates back and forth at the pore transition with a high bending angle before accessing a new pore at the SWCNT end. During reptation, the SWCNT is continuously undulating while sampling the accessibility of other pores. When the SWCNT reaches an accessible pore transition, the bending angle allows the SWCNT to diffuse into the new straight pore (cyan area, Fig. 6(a)). This effect of cross-pore bending angle will be further studied in future work exploring the bending energy landscape of SWCNTs in porous media.

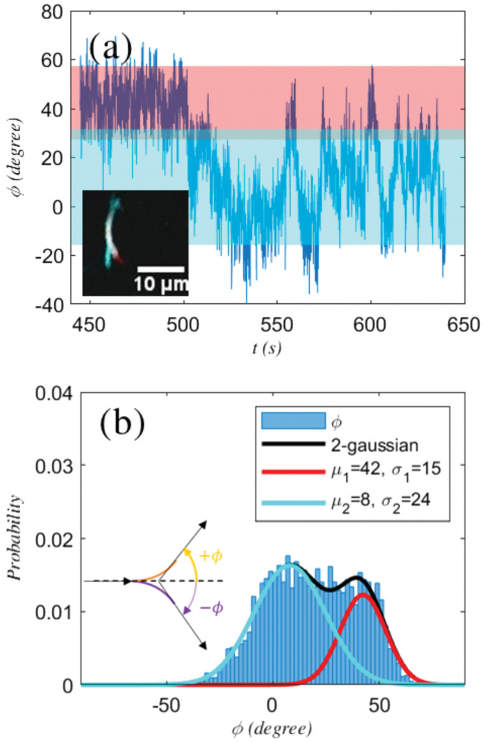

Fig. 6 SWCNT bending angle (ϕ) tracking in packed-colloid pores. (a) Bending angle tracking of SWCNT diffusing from pore transition (red block) to one straight pore (cyan block). Inset: False coloured SWCNT trajectory overlapping. Red marks straight pore location and green marks pore transition. (b) Bending angle distribution.

We further study the pore location and shape effect on SWCNT orientation and angular displacement (Fig. 7(a)–(c)) and the parallel and perpendicular translation with corresponding diffusions (Fig. 7(d)–(f)) of the same SWCNT in Fig. 7 but for a longer tracking duration. Inset image of Fig. 7(f) shows that the SWCNT first diffuses from a 42 degree pore transition (red area) to a straight pore (cyan area). Between these two regions, the SWCNT moves through the straight pore as it approaches the transition (white area in Fig. 7).

In this example, we observe three types of pore structures: pore-transition where the highly bent SWCNT ends locate at two straight pores of different orientations (red area), straight pore ends where the SWCNT moves back and forth between pore transition and the new straight pore (white area), and straight pore center where the SWCNT fully enters the new straight pore (cyan area). The straight pore center (cyan area) shows orientation confinement on both rotation and molecular bending, which shows a noisy plateau at the pore orientation (Fig. 7(a)) and bending angle (dotted line Fig. 7(b)) with a close to zero average bending angle (Fig. 7(b)). The power law index of the normalized MSAD in the straight pore confinement falls below 1, which indicates high rotational confinement in a straight packed-colloid pore (Fig. 7(a)). This pore confinement yields anisotropic hindrance on parallel and perpendicular translation. The perpendicular motion (n) in the straight pore is frozen, while parallel motion diffuses back and forth (Fig. 7(d)). Hence, the parallel time averaged MSD (TA-MSD, $\delta_s^2/\langle\delta_s^2\rangle$) fluctuates significantly while the perpendicular TA-MSD ($\delta_n^2/\langle\delta_n^2\rangle$) is close to zero (Fig. 7(e)).

At pore transitions (red region), the SWCNT bends between two pores with different orientations. Thus, the SWCNT bending angle shows a non-zero noisy plateau in the bending angle tracking (Fig. 7(b)) with a 42 degree average bending angle (Fig. 7(b)). Transitioning between two pores at different orientations corresponds to a high TA-MSAD ($\delta_\theta^2/\langle\delta_\theta^2\rangle$) at pore transition (red region in Fig. 7(c)). Hence, rotation coupled to

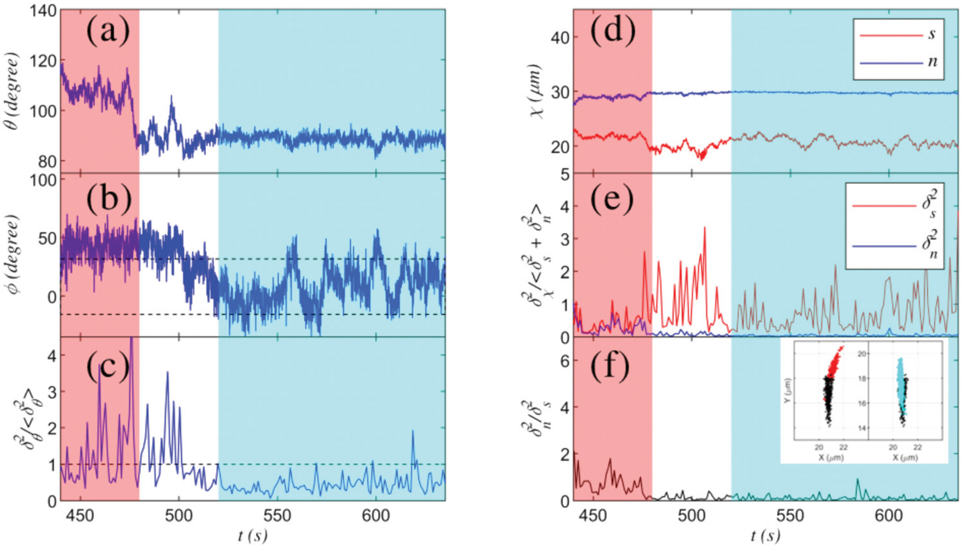

Fig. 7 SWCNT reptation motion tracking in packed-colloid porous media. (a)–(c) Angular motion tracking. (d)–(f) Translational motion tracking. Cyan area is a straight pore example. Red area is pore-transition. White area reflects straight pore that is close to pore transition. Inset (f) shows the COM of the straight pore to pore transition procedure. The left inset shows the COM from red to white region (black dots); right shows the region from white (black dots) to cyan area.

perpendicular motion (Fig. 7(d)) shows an accelerated perpendicular TA-MSD compared to the pore center region (Fig. 7(e)). At the same time, SWCNT parallel motion is hindered with lower parallel TA-MSD compared with the straight pore center region (Fig. 7(e)).

The white region in Fig. 7 shows the SWCNT diffusing into a straight pore center from the pore transition. In this case, SWCNT orientation aligns with the destination pore orientation, and the SWCNT bending angle decreases and fluctuates around zero under the straight pore confinement (Fig. 6(b)). The SWCNT TA-MSAD from the partially-confined SWCNT is higher than in the full confinement of the straight pore. However, in this observation, SWCNT parallel TA-MSD of partial pore confinement is closer to that in a straight pore than that in a pore transition. Furthermore, the SWCNT COM of each location is displayed in the inset of Fig. 7(f). The pore transition area (red) has a large curvature and thus confines the SWCNT to a highly bent conformation. The pore curvature effect leads to a significantly lower parallel TA-MSD (Fig. 7(e)) and higher translational anisotropic ratio of perpendicular and parallel TA-MSD (Fig. 7(f)) than at the non-pore transition pore site. While in the straight pore (cyan COMs) and partially straight pore (black COMs), SWCNT reptates along the orientation of target straight pore with much smaller pore confinement at the perpendicular direction. Straight pores limit the SWCNT COM perpendicular range to the pore size. While in a curved pore moving through pore transition, the SWCNT's perpendicular motion range increases significantly. In conclusion, the transport properties of stiff semiflexible filaments are dominated by the distribution of pore throat orientations at pore junctions, which dictates the curvature of the filament during inter-pore transitions.

Conclusions

SWCNTs in tightly confined porous media diffuse along the pore path and enter new pores by reorienting themselves by bending induced by chain thermal fluctuations. Although the motion is still reptational, the discrete and pre-set distribution of pore sizes and orientations controls chain dynamics and loosens the coupling of parallel and perpendicular MSDs; this differs from reptation in gel pores, where SWCNTs can bend around multiple, thin, fluctuating gel strands and diffuse along tortuous paths where parallel and perpendicular MSDs are coupled and display a characteristic 3/4 power law. SWCNTs in the heterogenous pores of packed colloids have their own peculiar dynamics. When motion is confined to a single straight pore, the SWCNTs' perpendicular mobility is significantly limited by the pore walls while the parallel mobility is only slightly reduced. Hence, parallel MSD shows thermal fluctuations with a 3/4 power law, while the perpendicular MSD remains the same size of the straight pore diameter before traversing into another straight pore.

Gels have high porosity ($\geq$98 v/v%);[43] their pore structure is tortuous and SWCNTs essentially create their own pores by slaloming around gel network strands. Conversely, randomly packed colloids have low porosity ($\sim$34 v/v%) and interconnected pores with different orientations and tortuosity; SWCNTs must bend at discrete, prescribed angles to access these pores. Moreover, the pore structure is spatially heterogeneous. Even for long observation times, we observe wide, location-dependent variability of the number of SWCNT disentanglements from one pore to the next. Locations where pore junctions provide numerous widespread pore orientations display normal SWCNT rotational diffusion; locations with more limited pore orientations lead to strong rotational confinement and subdiffusive rotational diffusion.

SWCNT stiffness plays a role *via* the higher (or lower) energy required to attain a specific bending angle. At pore transitions with different orientations, we observe that SWCNTs enter new pores whenever thermal fluctuations produce a sufficient bending angle to navigate the orientational change. The amplitude of such bending angle further helps to categorize heterogeneous pore locations into classes: straight pore center, straight pore end, and transition across pores. The observed rotational and translational TA-MSD are distinctly different in these pore classes.

Via single-molecule photoluminescence imaging, we accurately track SWCNT motion in porous media and show how location-dependent pore structure and SWCNT flexibility combine to control rotational and translational diffusion. This new method and model system offer a powerful tool for studying semiflexible filament motion in complex media beyond gels.[19,44,45] This novel physical understanding will impact the development of applications of semiflexible molecules in heterogenous porous media, such as SWCNT separations,[10,12] and the development of electromagnetically active rod-like nanorobots for reservoir *in-situ* sensing.[26,46,47]

Conflicts of interest

There are no conflicts to declare.

Acknowledgements

This research was financially supported by Welch Foundation grant C-1668. FCM was supported in part by the National Science Foundation Division of Materials Research (Grant DMR1826623) and the Center for Theoretical Biological Physics (Grant PHY2019745). L. C. acknowledges funding from the European Research Council (ERC) under the European Union's Horizon 2020 research and innovation program (grant agreement no. 951284). We thank Robert Pinnick, Robert Headrick and Hagen Eckert for helpful suggestions.

Notes and references

1 M. Doi and S. F. Edwards, *J. Chem. Soc., Faraday Trans. 2*, 1978, **74**, 1789–1801.
2 P. G. de Gennes, *J. Chem. Phys.*, 1971, **55**, 572–579.

3 M. Doi and S. F. Edwards, *The Theory of Polymer Dynamics*, Clarendon Press, 1988.

4 T. C. B. McLeish, *Adv. Phys.*, 2002, **51**, 1379–1527.

5 R. Everaers, *Science*, 2004, **303**, 823–826.

6 D. E. Smith, T. T. Perkins and S. Chu, *Phys. Rev. Lett.*, 1995, **75**, 4146–4149.

7 J. Käs, H. Strey and E. Sackmann, *Nature*, 1994, **368**, 226–229.

8 B. Wang, J. Guan, S. M. Anthony, S. C. Bae, K. S. Schweizer and S. Granick, *Phys. Rev. Lett.*, 2010, **104**, 118301.

9 M. Keshavarz, H. Engelkamp, J. Xu, O. I. van den Boomen, J. C. Maan, P. C. M. Christianen and A. E. Rowan, *J. Phys. Chem. B*, 2017, **121**, 5613–5620.

10 C. Y. Khripin, X. Tu, J. M. Heddleston, C. Silvera-Batista, A. R. Hight Walker, J. Fagan and M. Zheng, *Anal. Chem.*, 2013, **85**, 1382–1388.

11 E. Farkas, M. Elizabeth Anderson, Z. Chen and A. G. Rinzler, *Chem. Phys. Lett.*, 2002, **363**, 111–116.

12 X. Huang, R. S. Mclean and M. Zheng, *Anal. Chem.*, 2005, **77**, 6225–6228.

13 Z. Mokhtari and A. Zippelius, *Phys. Rev. Lett.*, 2019, **123**, 028001.

14 N. Fakhri, F. C. MacKintosh, B. Lounis, L. Cognet and M. Pasquali, *Science*, 2010, **330**, 1804–1807.

15 L. Deng, X. Trepat, J. P. Butler, E. Millet, K. G. Morgan, D. A. Weitz and J. J. Fredberg, *Nat. Mater.*, 2006, **5**, 636–640.

16 J. Liu, M. L. Gardel, K. Kroy, E. Frey, B. D. Hoffman, J. C. Crocker, A. R. Bausch and D. A. Weitz, *Phys. Rev. Lett.*, 2006, **96**, 118104.

17 J. Käs, H. Strey, J. X. Tang, D. Finger, R. Ezzell, E. Sackmann and P. A. Janmey, *Biophys. J.*, 1996, **70**, 609–625.

18 J. L. Bitter, Y. Yang, G. Duncan, H. Fairbrother and M. A. Bevan, *Langmuir*, 2017, **33**, 9034–9042.

19 C. P. Brangwynne, G. H. Koenderink, F. C. MacKintosh and D. A. Weitz, *Phys. Rev. Lett.*, 2008, **100**, 118104.

20 P. Lang and E. Frey, *Nat. Commun.*, 2018, **9**, 494.

21 S. Leitmann, F. Höfling and T. Franosch, *Phys. Rev. Lett.*, 2016, **117**, 097801.

22 N. Fakhri, *Single-Walled Carbon Nanotube Dynamics Simple and Complex Media*, PhD thesis, Rice University, 2011.

23 B. Chakrabarti, C. Gaillard and D. Saintillan, *Soft Matter*, 2020, **16**, 5534–5544.

24 A. Koponen, M. Kataja and J. Timonen, *Phys. Rev. E: Stat. Phys., Plasmas, Fluids, Relat. Interdiscip. Top.*, 1997, **56**, 3319–3325.

25 M. M. Roozbahani, R. Borela and J. D. Frost, *Materials*, 2017, **10**, 1237.

26 M. J. Kadhum, D. P. Swatske, C. Chen, D. E. Resasco, J. H. Harwell and B. Shiau, *Propagation of Carbon Nanotube Hybrids through Porous Media for Advancing Oilfield Technology*, The Woodlands, Texas, USA, 2015, p. 10.

27 T. Bhattacharjee and S. S. Datta, *Nat. Commun.*, 2019, **10**, 2075.

28 C. A. Dyke, M. P. Stewart and J. M. Tour, *J. Am. Chem. Soc.*, 2005, **127**, 4497–4509.

29 Y. Zeng and D. J. Harrison, *Anal. Chem.*, 2007, **79**, 2289–2295.

30 D. J. Norris, E. G. Arlinghaus, L. Meng, R. Heiny and L. E. Scriven, *Adv. Mater.*, 2004, **16**, 1393–1399.

31 H. Gui, H. Chen, C. Y. Khripin, B. Liu, J. A. Fagan, C. Zhou and M. Zheng, *Nanoscale*, 2016, **8**, 3467–3473.

32 D. A. Tsyboulski, S. M. Bachilo and R. B. Weisman, *Nano Lett.*, 2005, **5**, 975–979.

33 F. Gittes, B. Mickey, J. Nettleton and J. Howard, *J. Cell Biol.*, 1993, **120**, 923–934.

34 F. A. L. Dullien, *Porous Media: Fluid Transport and Pore Structure*, Academic Press, 2012.

35 S. L. Bryant, P. R. King and D. W. Mellor, *Transp. Porous Media*, 1993, **11**, 53–70.

36 R. Granek, *J. Phys. II*, 1997, **7**, 28.

37 Y. Han, A. M. Alsayed, M. Nobili, J. Zhang, T. C. Lubensky and A. G. Yodh, *Science*, 2006, **314**, 626–630.

38 F. Gittes and F. C. MacKintosh, *Phys. Rev. E: Stat. Phys., Plasmas, Fluids, Relat. Interdiscip. Top.*, 1998, **58**, R1241–R1244.

39 D. C. Morse, *Macromolecules*, 1998, **31**, 7044–7067.

40 E. Farge and A. C. Maggs, *Macromolecules*, 1993, **26**, 5041–5044.

41 T. Odijk, *Macromolecules*, 1983, **16**, 1340–1344.

42 I. Teraoka, K. H. Langley and F. E. Karasz, *Macromolecules*, 1992, **25**, 6106–6112.

43 A. Pluen, P. A. Netti, R. K. Jain and D. A. Berk, *Biophys. J.*, 1999, **77**, 542–552.

44 C. P. Brangwynne, G. H. Koenderink, F. C. MacKintosh and D. A. Weitz, *J. Cell Biol.*, 2008, **183**, 583–587.

45 C. P. Brangwynne, F. C. MacKintosh and D. A. Weitz, *Proc. Natl. Acad. Sci. U. S. A.*, 2007, **104**, 16128–16133.

46 H. Zhou, C. C. Mayorga-Martinez, S. Pané, L. Zhang and M. Pumera, *Chem. Rev.*, 2021, **121**, 4999–5041.

47 J. G. Duque, M. Pasquali and H. K. Schmidt, *J. Am. Chem. Soc.*, 2008, **130**, 15340–15347.